Laser and Particle Beams (2000), *18*, 25–35. Printed in the USA.

Interaction experiments of laser light with low density supercritical foams at the AEEF ABC facility

A. CARUSO,[1] C. STRANGIO,[1] S.YU. GUS'KOV,[2] AND V.B. ROZANOV[2]

[1]Associazione EURATOM-ENEA sulla Fusione, C.R.E. Frascati. Via E. Fermi 45, C.P. 65, 00044 Frascati, Roma, Italia
[2]P.N. Lebedev Physical Institute, Leninsky Prospect 53, 117924 Moskow, Russia

(RECEIVED 4 February 1999; ACCEPTED 4 February 1999)

Abstract

Experiments have been performed on the interaction physics of laser light with polystyrene and agar–agar foams having average densities higher than critical. The experiments have been performed at the ABC facility of the Associazione EURATOM-ENEA sulla Fusione, in Frascati. The main addressed topics have been energy coupling (balance), diffusion of energy into the target, plasma and dense phase dynamics, and harmonics generation. The laser light ($\lambda = 1.054\ \mu$m) was focused by a F/1 lens to produce on the target surface about 1.6×10^{14} W/cm^2 ($\approx 10^{15}$ W/cm^2 in the waist, set about 100 μm inside the target). Experiments have shown efficient energy coupling (>80%) to be attributed to cavity formation in the low density foam (efficient light absorption) and good mechanical coupling of the plasma trapped in the cavity to the dense phase (ablation pressure work). Heat diffusion possibly plays a transitory role in the initial stages of the interaction (300–500 ps). Time integrated harmonics measurements revealed a blue-shifted 2ω and a red-shifted $5/2\omega$.

1. INTRODUCTION

We shall present experiments on the interaction of circularly polarized laser light ($\lambda = 1.054\ \mu$m) with structured low-Z materials having an average density of $\bar{\rho} = 5$–10 mg/cm^3 (polystyrene foams, agar-agar). This density is somewhat higher than the critical one for the used light wavelength ($\rho_c \approx 3$ mg/cm^3 at $\lambda = 1.054\ \mu$m). The experiments have been performed at the ABC facility of the Associazione EURATOM-ENEA sulla Fusione, in Frascati. ABC is powered by a two-beam Nd laser delivering up to 100 + 100 J in about 3 ns.

For the foams with cellular structures used in the experiments (polystyrene), the cell radius scales as $r \propto (\rho_0/\bar{\rho})\Delta$, where ρ_0 is the wall material density and Δ is the wall thickness. Experiments have been performed also on agar–agar, which has a roughly filamentary structure. In this case, filaments distance scale as $r \propto (\rho_0/\bar{\rho})^{1/2} d$, where d is the filaments diameter. Typically, $2r = 75$–$150\ \mu$m and the thickness of the target used was $\approx 10 \times 2r$. Samples of the materials are seen in Figure 1. Typical targets had a parallelepiped shape, and a F/1 lens was used to focus the laser light, according to the geometry indicated in Figure 2a.

Address correspondence and reprint requests to: A. Caruso, Associazione EURATOM-ENEA sulla Fusione, CRE Frascati, Via E. Fermi 45, CP 65, 00044 Frascati, Roma, Italy. E-mail: caruso@frascati.enea.it

Typical maximum power density on the average front surface was $\approx 1.6 \times 10^{14}$ W/cm^2 ($\approx 10^{15}$ W/cm^2 in the waist) on an area of about 100 μm in diameter. The normalized laser power waveform was represented in Figure 2b.

Due to the discrete nature of the target, the concept of front surface has a statistical meaning (depending on the focus site, the cell being open or closed). For the conditions of sharp focusing adopted in the experiment, the first solid element irradiated was located in a position uncertain in depth by at least $2r = 75$–$150\ \mu$m.

In the case of filamentary structures (agar-agar) the first initially irradiated filament is on the average at a depth $(\rho_0/\bar{\rho})^{1/2} r$ (see Gus'kov & Rozanov, 1997). This depth can be even greater than the target thickness. So, for cell-structured materials the laser spark can be initiated in a site that can result well inside of the material (of the order of $2r$, e.g., near the beam waist). For filamentary structures, filaments in a depth $\approx 30r$ can be initially irradiated.

When the material starts to be irradiated by a high power laser light, the solid components (walls or filaments) are exploded, and a void closure process is initiated. This process lasts for a sizeable time, $t = r/V$ (V is the explosion velocity), during which a highly nonequilibrium state can be created. The time t can be estimated as follows. Being the average density $\bar{\rho}$ supercritical, during the void closure the exploding material never becomes transparent. The collected energy can be evaluated as $\approx \phi \times \sigma \times$

https://doi.org/10.1017/S0263034600181042 Published online by Cambridge University Press

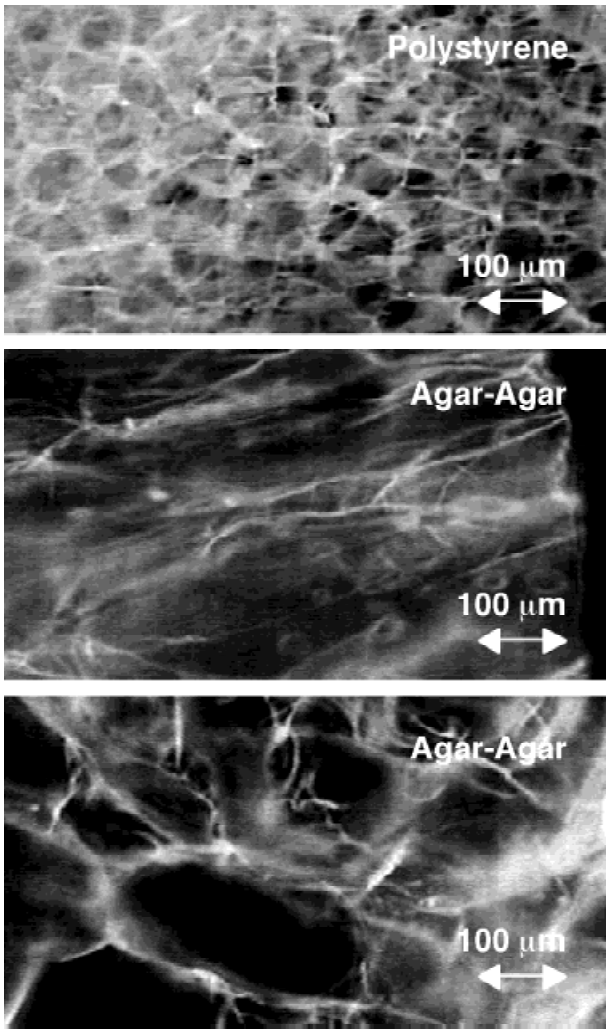

Fig. 1. Microscopic views of the foams used in the ABC experiments. The agar–agar views refer to different material alignments.

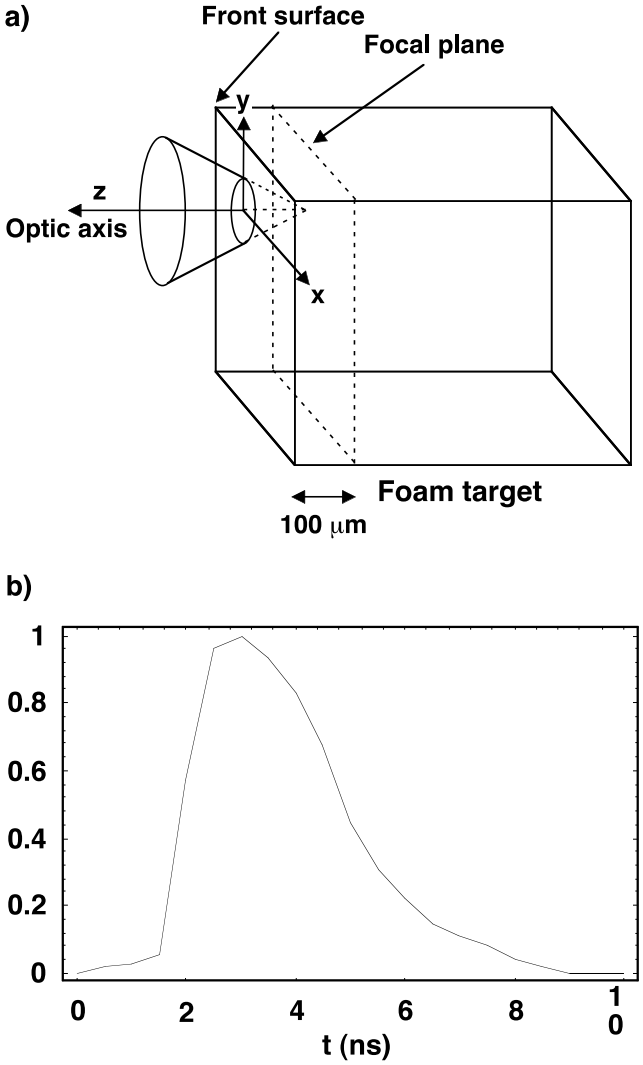

Fig. 2. (a) Focusing geometry on the foam blocks used in the experiments. Typically the optic axis was set ≈200 μm below the target top surface. (b) Waveform of the laser pulses used in the experiments.

(r/V), where σ is the cell cross-section ($\sim r^2$ for cells, r for filaments) and ϕ the absorbed power flux density. As $\sigma \times r$ is, a part from a geometric factor g, the volume to be filled by the exploding material, the energy stored during the closure process is roughly $\phi \times g \times$ volume/V. This quantity is to be equated to mass $\times$ $(V^2/2 + \epsilon_e)$, where $\epsilon_e = ZT_e/(\gamma - 1)m_i$ is electronic energy per unit mass, Z the ionic charge, T_e the electronic temperature, m_i the ionic mass, and γ an adiabatic index. From momentum conservation ($\bar{\rho} \times V^2/r \approx$ pressure/r) it follows that $V^2 \approx (\gamma - 1)\epsilon_e$. Since $\bar{\rho} =$ mass/volume, we get $V \approx (\phi/3\bar{\rho})^{1/3}$ [assuming $2g(\gamma - 1)/(\gamma + 1) \approx 1/3$]. The relaxation time ($t_{\text{relax}}$) of the electron–ion mixture to the same temperature can be evaluated by using $V^2 \approx (\gamma - 1)\epsilon_e$. The ion–ion collision mean free path l_{ii} is featured by a fast dependence on V and $\bar{\rho}(\propto V^4/\bar{\rho})$, or $l_{ii} \propto \phi^{4/3}/\bar{\rho}^{7/3}$. The relaxation time scales as $t_{\text{relax}} \propto \phi/\bar{\rho}^2$. Note that l_{ii} has to be properly averaged for a mixture of ions all colliding at the velocity V. For polystyrene, numerical estimates are displayed in Table 1, where $t = r/V$ was computed for $r =$ 100 μm and the Coulomb logarithm was set equal to 5.

For both the considered densities, at power fluxes not greater than 10^{14} W/cm^2, the ionic gas is collisional and

Table 1. *Estimates for the kinetics of the initial nonequilibrium stages of a polystyrene foam irradiated by laser light.*

ϕ (W/cm^2)	$\bar{\rho}$ (mg/cm^3)	V (cm/s)	t (ns)	t_{relax} (ns)	l_{ii} (μm)
10^{13}	10	1.5×10^7	0.67	0.11	0.051
10^{14}	10	3.2×10^7	0.31	1.1	1.1
10^{15}	10	6.9×10^7	0.14	11	24
10^{13}	20	1.2×10^7	0.84	0.02	0.010
10^{14}	20	2.6×10^7	0.39	0.28	0.22
10^{15}	20	5.5×10^7	0.18	2.8	4.7

https://doi.org/10.1017/S0263034600181042 Published online by Cambridge University Press

accretion shocks can damp the hydrodynamic motion. Furthermore, relaxation to a single temperature occurs during this process. However, smaller amplitude density oscillations can persist for a time much longer than $t = r/V$, since the viscosity damping time is $t_{\rm osc} \approx t \times 3r/l_{ii}$. For larger ϕ the ion–ion collisions becomes more rare (in the reference time t), but damping can occur due to phase mixing with contiguous cells, and interpenetrating beams electrostatic instabilities.

After the transitory phenomena previously described, a continuous fluid model can be used to describe the main hydrodynamics features. The Frascati three temperatures, hydrodynamic code CoBi3 was used to simulate conditions similar to the experiments described in this paper. CoBi3 is a Lagrangian code in which ray tracing describes laser light propagation, and a real matter equation of state is used. In the simulations the focusing conditions and the laser waveform described in Figure 2a and Figure 2b were adopted, and polystyrene at $\bar{\rho} = 10$ mg/cm^3 was assumed as target material. Some results of these simulations are shown in Figure 3. The main hydrodynamic feature is the formation in the target, at the end of the high power laser ramp, of a cavity filled by plasma at subcritical density. In this cavity the light penetrates, and the rays are refracted and trapped. Reflected rays mostly remain in the focusing lens cone. A thin layer, with a density 10 times the initial material density and moving at a velocity of $\approx 10^7$ cm/s, wraps the cavity. The shape of this layer remains self-similar in time, until target passing-through occurs. Typically, the ratio of the cavity entrance radius to its axial length is about 0.4. Large laser light absorption was found for the described simulation (that is $>70\%$ at $\lambda = 1.054$ μm).

The general hydrodynamic parameters can be estimated by an ablation-pushed snowplow model, in which the momentum equation reads $\bar{\rho}R^2/t^2 \approx \rho_{\rm plasma}\epsilon_{\rm plasma}$ (R is the cavity radius, $\rho_{\rm plasma}$ the density of the plasma enclosed within, $\epsilon_{\rm plasma}$ its specific energy). The system is closed by the energy balance equation, and by an absorption matching condition for R (for inverse bremsstrahlung $a\rho^2_{\rm plasma}R/\epsilon^{3/2}_{\rm plasma} \approx 1$, where $a \approx 8 \times 10^{28}\ \lambda^2_{\mu\rm m}$ for polystyrene and $\lambda_{\mu\rm m}$ is the laser wavelength). It is to be noted that in the framework of this model it is not possible to obtain, by dimensional methods, a definite dependence for the main quantities, as a pure number can be formed by combining $\bar{\rho}$, a, t, and the laser power w. So, in order of magnitude estimates, it is possible to write the energy balance in two alternative ways, that is $wt \approx \rho_{\rm plasma}\epsilon_{\rm plasma}R^3$ or $w \approx \rho_{\rm plasma}\epsilon^{3/2}_{\rm plasma}R^2$. If the first dependence is adopted, it is found that $\rho_{plasma}/\epsilon^{3/2}_{plasma}R^2/w \approx a^{1/7}t^{9/35}\bar{\rho}^{12/35}/w^{2/35}$, a quantity about unity for the Frascati experiment. Due to very slow dependence on $\bar{\rho}$, a, t, and w, it is clear that this result is quite general, and for order of magnitude estimates it is immaterial which balance of energy is adopted.

2. DIAGNOSTIC SET-UP

The standard diagnostic ABC equipment was used for the study presented in this paper. The diagnostics layout is shown

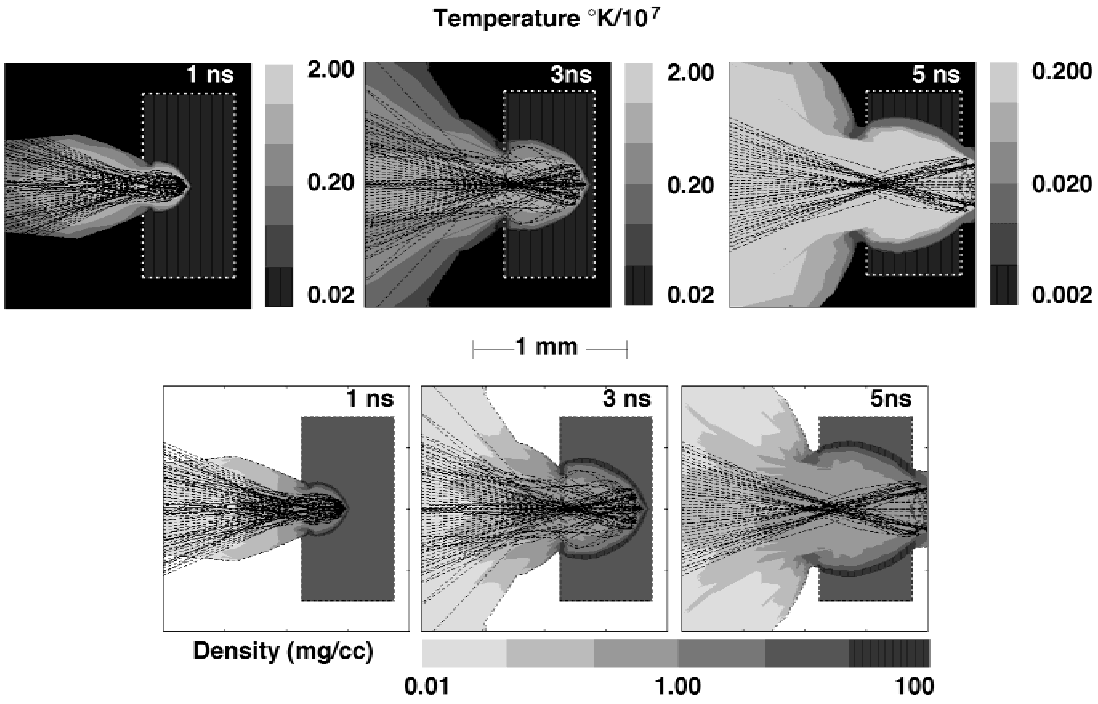

Fig. 3. Hydrodynamic simulation for a polystyrene target at initial average density $\bar{\rho} = 10$ mg/cm^3. Laser and focusing conditions were those described in Figure 2. The times were evaluated from the beginning of the laser high power ramp. The 3T, 2D Lagrangian hydrodynamic code CoBi3 of the AEEF was used to perform the simulations.

https://doi.org/10.1017/S0263034600181042 Published online by Cambridge University Press

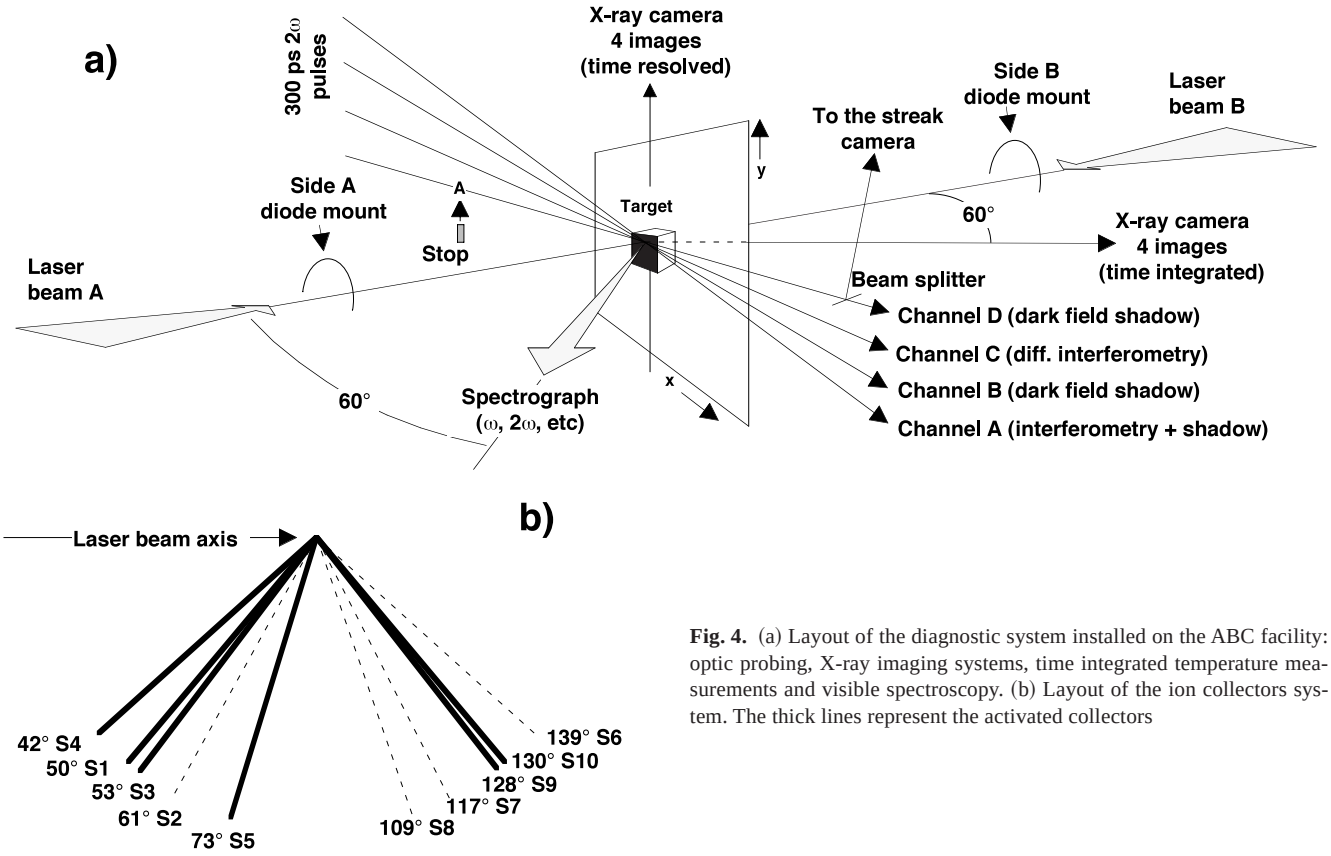

Fig. 4. (a) Layout of the diagnostic system installed on the ABC facility: optic probing, X-ray imaging systems, time integrated temperature measurements and visible spectroscopy. (b) Layout of the ion collectors system. The thick lines represent the activated collectors

in Figure 4a and Figure 4b. Of the two beams of ABC, the beam A was used as the driver in the experiments.

The X-ray-framing camera for top-views was operated according to the scheme described in Figure 5 (where some relevant camera parameters are also given). Imaging at different times is obtained by properly delayed individual activation of the strips, on which the different target positions are imaged, see also Strangio & Caruso, 1998. Four time-integrated X-ray images were taken by pinhole imaging from the rear side of the target, through different filters and at 120° to the front surface target normal.

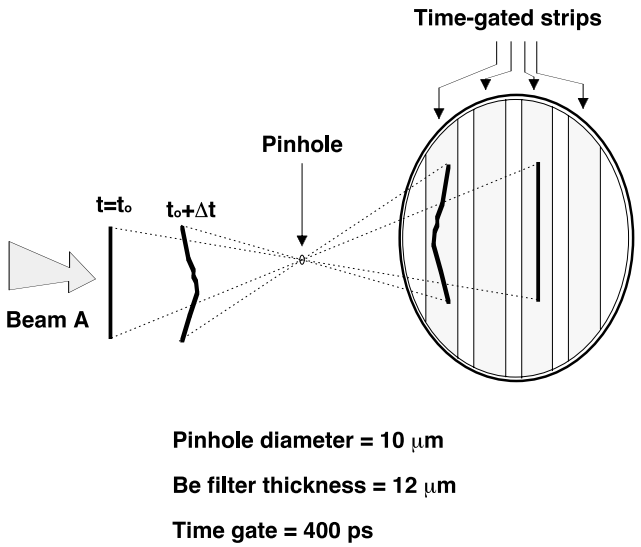

Fig. 5. Soft X-ray time-resolved imaging system. Images at different times are obtained by polarizing the channel-plate strips with differently delayed electric pulses.

The thick lines in Figure 4b represent the angle of the Faraday cups actually activated in the experiment. Collectors at near angles have been activated to investigate the fluctuations in angular dependence. The digital electric signal was processed to find the velocity distribution function discussed in this paper.

The optical diagnostics are based on probing by four synchronized, 2ω light pulses (duration $\approx$ 300 ps). The pulses used for this are produced by successive splitting the ABC preamplifier beam, by doubling the frequency, and by electro-optic slicing. Dark-field shadographies and interferograms (normal and differential) based on wave splitting by Wollaston prisms (see Benattar *et al.*, 1979), are provided by these diagnostics.

The light emitted by the target was registered by a streak-camera in the visible, set on the channel D of the optical diagnostics assembly. A stop inserted at the point A was used to remove the optical short pulse. However, dark field shadographies may result on the channel D due to in-scattering, by the target, of light of the contiguous channel C (cross talking).

https://doi.org/10.1017/S0263034600181042 Published online by Cambridge University Press

The filter method (Ni foils in this experiment) was used to measure the temperature by X-ray detection (see Elton, 1968, Caruso & Strangio, 1985). The signal was taken by four semiconductor diodes mounted in front of the target (side A mount, see Fig. 4a), and by four diodes mounted behind the target (side B mount). For the mount B filters, filtering due to the target was included in the calculations.

The high-resolution visible spectrograph, set at 60° to the target normal, recorded time-integrated, wide-angle scattered light.

3. EXPERIMENTAL RESULTS

Unless otherwise stated, the following results refer to experiments performed on polystyrene targets at an average density $\bar{\rho} = 10$ mg/cm^3. The focusing conditions were those described in Figure 2a, the optic axis impinging on the target surface ≈200 μm below the target top surface.

A typical transverse-view streak camera record, taken along the channel D and with streak slit aligned along the laser optical axis (see Fig. 4a), is shown in Figure 6. The discharge starts near the laser beam waist, inside the target. Its front moves towards the irradiated target surface at a velocity $V_z \approx 5 \times 10^7$ cm/s (see Fig. 2a for the coordinate convention).

A slower process proceeds into the target at a velocity $V_z \approx -3.7 \times 10^7$ cm/s. The process is quenched after about 900 ps, when a much slower front detaches from the fireball and proceeds into the target at a velocity $V_z \approx -6$–9×10^6 cm/s.

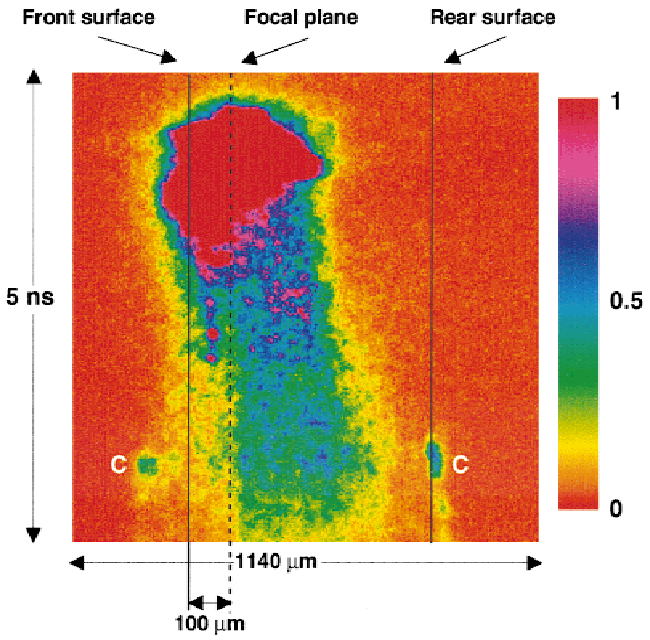

Fig. 6. Visible streak-camera record for a shot on a polystyrene target at density $\bar{\rho} = 10$ mg/cm^3. The focusing conditions were those indicated in Figure 2a. The laser power density was 1.6×10^{14} W/cm^3 on the front surface and ≈ 10^{15} on the waist.

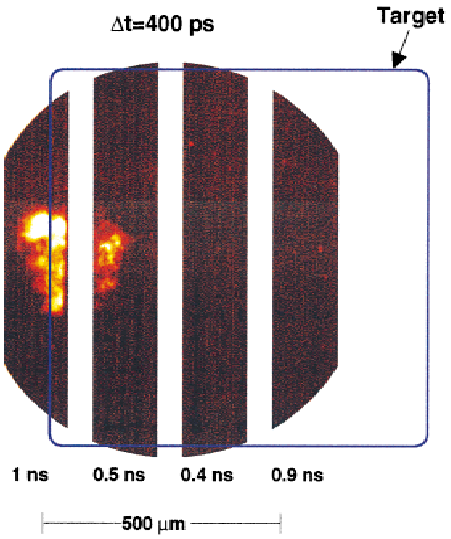

Fig. 7. Top view soft X-ray imaging of a polystyrene target irradiated according to the conditions indicated in Figure 6.

The bright spots marked by C are due to the channel C probing beam scattered by the target in the streak channel (D).

A time-resolved X-ray image is shown in Figure 7. The times marked under the strips are the activation times of each strip. These times are relative to one ($t = 0$) for which the X-ray signal is very faint (the beginning of the high power laser pulse ramp, see Fig. 2b). It is seen that a bright spot is formed in the first 500 + 400 ps, and the depth of this feature corresponds, more or less, to that seen by visible streak measurements. Also, it is seen that in 900 − 500 ps (4th strip time minus second strip time) the emitting region doesn't reach the 4th strip ≈ 300 μm away from the fireball.

The localization of the X-ray emission within a spot not greater than 200 μm is confirmed also by the four time-integrated X-ray images taken from the rear side of the target. The situation is not material or laser energy dependent. In Figure 8 are shown the images taken for a shot on agar-agar ($\bar{\rho} = 5$ mg/cm^3), at a laser energy (and power densities) a factor 1.75 greater than that used for the shots on polystyrene presented in this paper.

These results show that in the regime of the performed experiments, no substantial supersonic heat diffusion occurs. This is in agreement with heat diffusion estimates based on classical electronic conduction in homogeneous media. It is easily found that (in 3D) heat diffusion is overrun by hydrodynamic expansion, in a time t_0 and on a length l_0 of the order of magnitude as those found in the experiment. Furthermore t_0 and l_0 scale slowly with the material density and the laser power ($t_0 \propto w^{3/11}/\bar{\rho}^{5/11}$ and $l_0 \propto w^{4/11}/\bar{\rho}^{3/11}$). For times greater than t_0 the X-ray emission per unit volume drops due to density decrease.

As already noted, polystyrene has a cellular structure with a typical size of the order of the depth at which the laser waist is placed (≈100 μm). About this size is the laser spot diameter on the target surface. A scenario for the initial interaction

https://doi.org/10.1017/S0263034600181042 Published online by Cambridge University Press

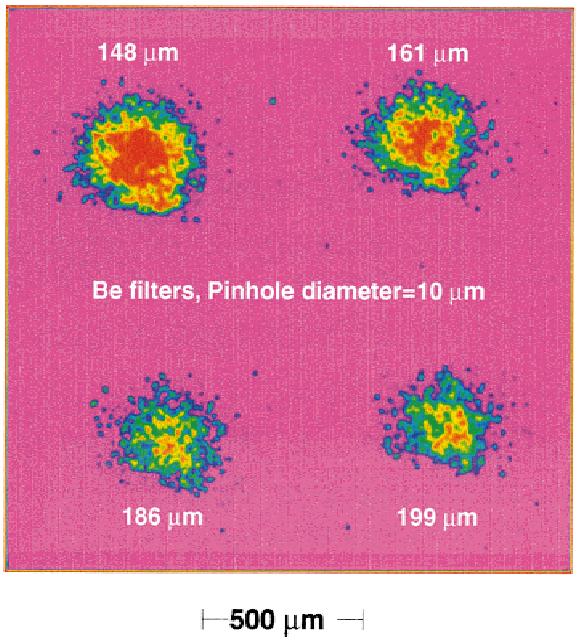

Fig. 8. Four pinholes time-integrated, rear side soft X-ray imaging. Shot on agar–agar target, at power densities a factor 1.75 greater than those used for polystyrene. The numbers indicate the Be filter thickness.

stages can be based on the following description. During the laser high power ramp, the wall surfaces of the few interacting cells are partially exploded in the void through the target surface, clearing the way to the light penetration (see, for self-consistency, the time t in Table 1). The cavity formed in this way is the seed for the cavity formation and the dynamics described in section 1.

Since density of the high temperature plasma filling the evolving cavity is lower than the initial material density (about a factor 30 less), the X-ray cavity imaging is not possible with a setup appropriate for the initial high-density stages. In this study, the cavity motion (snowplow) was observed by optic methods. As the laser radiation was focused just below the target top surface ($\approx$200 μm), the snowplow motion can be seen, by shadographies, as an advancing front on the top and on the front surfaces.

In Figure 9 optic imaging for one shot is displayed. The target, a cube of polystyrene (800-μm side) at $\bar{\rho} = 10$ mg/cm^3, was mounted on a 10-μm glass fiber. The times indicated in the figure are calculated from the starting of the high power laser ramp (see Fig. 2b).

The dark field shadography taken on channel B shows an advancing structure along the top and the front surfaces (front

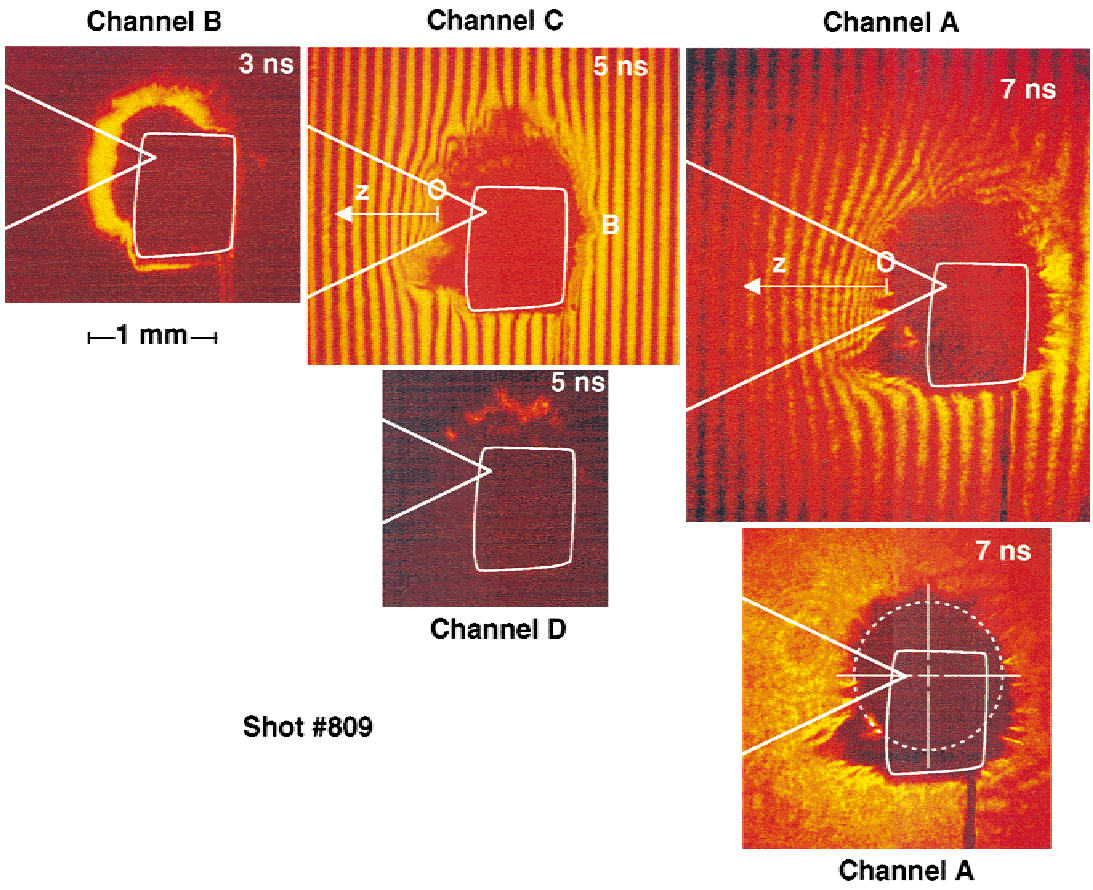

Fig. 9. Optic imaging of a shot on a polystyrene block at $\bar{\rho} = 10$ mg/cm^3 irradiated according to the standard conditions described in the text and in the Figure 6 caption.

https://doi.org/10.1017/S0263034600181042 Published online by Cambridge University Press

velocity $V_f \approx 8.5 \times 10^6$ cm/s). This structure can be considered as due to the previously discussed hydrodynamic feature advancing into the target, and perturbing the above mentioned surfaces (the ablation-pushed snowplow). It is also possible to infer this front to be somewhat pointed, due to the laser light channeling in the cavity (see, on channel C, the feature B on the rear target surface).

Channel D was closed by a stop set before the target (see Fig. 4a), to allow streak camera records in emitted light. Nevertheless, channel C-light, deflected by the most dense plasma regions on the top of the target, entered the channel D imaging optics, producing a dark field shadography. The shadow in channel A was provided, as by product, by the reference beam of the splitting front interferometer. This last shadow shows that the smooth structure seen in channel B evolves to a sort of highly structured spherical explosion around a point sited on the optic axis, about 200 μm behind the laser light waist. The explosion velocity is $\approx 8 \times 10^6$ cm/s and typical features are radial tiny jets.

The plasma density distribution outside the dense phase, that is up to the cavity entrance, has been deduced by processing the interferograms of channels C and A (see Fig. 9). For the electronic density, it has been assumed the space distribution with cylindrical symmetry $n_e(r,z) = n_{eo}(z) \times \exp[-r^2/R^2(z)]$ with $r^2 = x^2 + y^2$ and $R(z) = R_0 + az$ (see the interferograms in Fig. 9). The radius R_0 is deduced from the experiment and a is set 0.58, by comparison with numerical simulations. The remaining function $n_{eo}(z)$ is deduced from the fringes shift. Of the two interferometers, the one in channel C (5 ns delay) actually measures the quantity $d(\int n_e\, dl)/dz$, where the integral is taken along the line of sight. This is due to the small splitting angle of the Wollaston prism used to split the probing wave. The resulting equation has been integrated by setting to zero the density where the last detectable fringe displacement occurs. The larger splitting angle interferometer (on channel A, delay 7 ns) provides directly the density. The results of these measurements are shown in Figure 10. In the points O (both for channel C and A) the density turned out to be $n_{eo}(0) \approx 5.7 \times 10^{19}$ cm^{-3}. This value of the density can be indicative of a lower bound of the electronic density within the cavity n_{ecav} (from absorption matching conditions or numeric simulations it is expected $n_{\mathrm{ecav}} \approx 2\, n_{\mathrm{eo}}(0) \approx 10^{20}$ cm^{-3}). At the time 5 ns the total number of electrons in the external plasma was $N_{\mathrm{etot}} \approx 5 \times 10^{15}$, whereas at 7 ns $N_{\mathrm{etot}} \approx 8.5 \times 10^{15}$. Taking an average ionic charge $Z = 3.5$ it follows that the total ion number was, at 7 ns (that is after the end of the laser pulse), $N_{\mathrm{itot}} = N_{\mathrm{etot}}/Z \approx 2.4 \times 10^{15}$.

Time-integrated temperatures measurement taken with the filtered diode-set of the side A mount (see Fig. 4a) was consistent with a temperature of about 1 keV.

The transmission measurements taken on both the sides (A and B) were also assembled in a single plot, looking for the couple temperature-target C areal density giving the best fit. The best fitting couple was $T_e = 0.9$ keV and a C areal density of 0.45 mg/cm^2 (corresponding to about 490 μm of foam at the initial density).

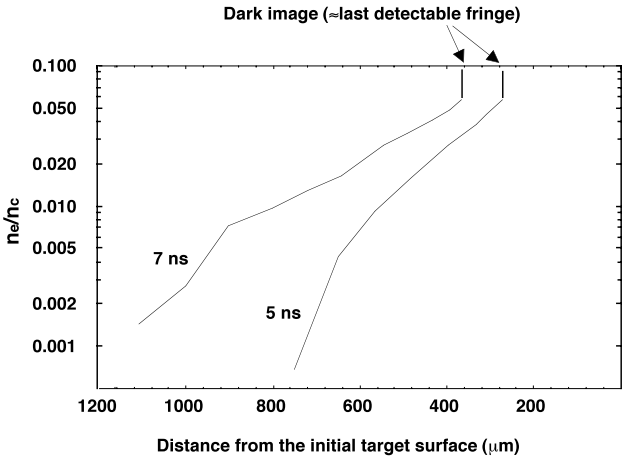

Fig. 10. Profile of electronic density as deduced from the interferograms of Figure 9.

Ion collection (Faraday cups) was performed according to the geometry displayed in Figure 4b. The cups plane contained the optic axis and was at an angle of 64.4° from the top view direction (see Fig. 4a). The activated cups were those marked by thick lines.

In Figure 11, the collected charge velocity distribution functions are displayed. Typical feature of these is the presence of two groups of particles associated with velocities of $\approx 4 \times 10^7$ cm/s and $\approx 1 \times 10^7$ cm/s. On some of the collectors the lowest velocity group appears as a stream (angles 50° and 130°).

It is to be noted how the signal can be substantially modified in shape by passing from a cup to another a few degrees nearer in angle (compare the 50° and the 52.5° signals, and the one for 127.5° with that for 130°). This result, associate to the low velocity group, is shot-to-shot erratic and may be connected with the tiny jets observed in the 7 ns shadography (channel A).

In the ABC installation, the assembly sketched in Figure 12 is used to measure the laser light energy reflected/transmitted in the cone of the focusing lenses. The result for reflected light in the foam experiments was 6–9% of the laser light. The transmitted light was 1–2%.

From numerical simulations and from experiments, most of the reflected light is expected to go through the focusing lens, because the ratio of the cavity entrance radius to its axial length is about 0.4. Then, from measurements, it is possible to conclude the absorbed energy to be nearly 90%.

Time-integrated harmonics measurements have been performed by the spectrometer set at 60° to the normal of the target, out of the focusing lens cone. The only detectable harmonics were 2ω and $(5/2)\,\omega$. The structure of these signals is reported in Figure 13a and in Figure 13b. The maximum of the 2ω spectrum is shifted by 12.7 Å towards the

https://doi.org/10.1017/S0263034600181042 Published online by Cambridge University Press

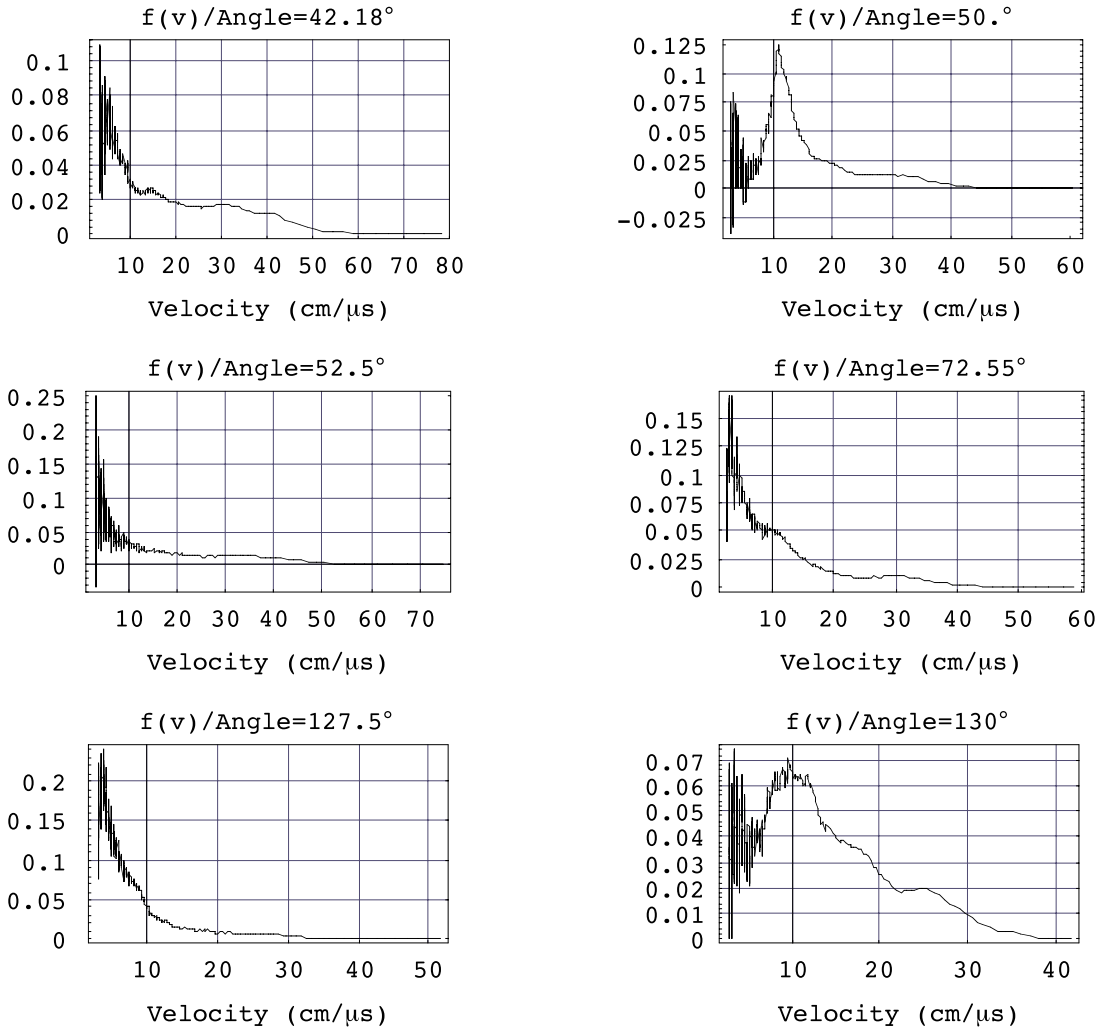

Fig. 11. Ion charge velocity distribution functions as seen by the Faraday cups aligned according to the scheme of Figure 4b.

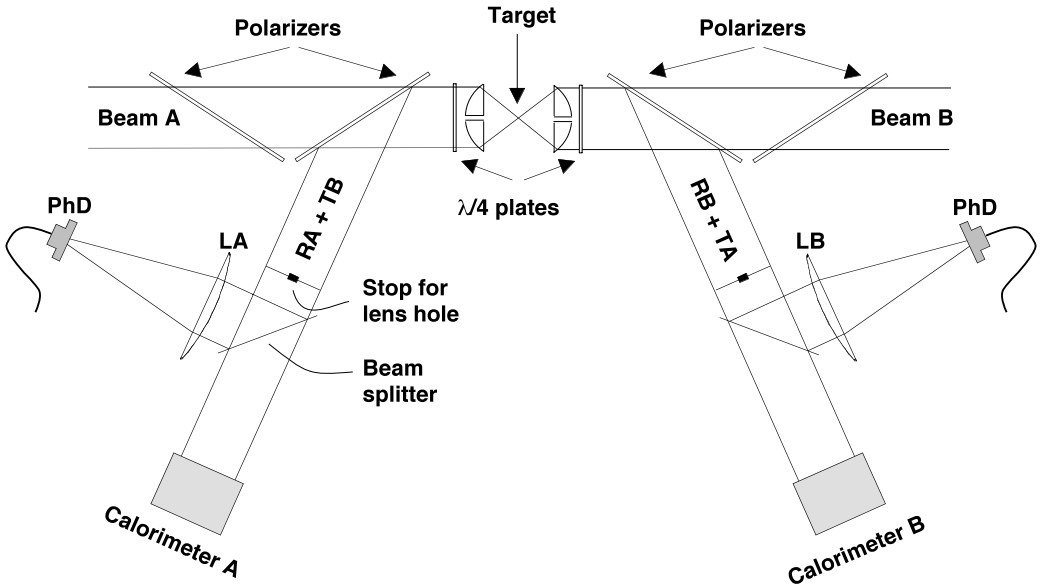

Fig. 12. ABC assembly for transmitted/reflected light measurements.

https://doi.org/10.1017/S0263034600181042 Published online by Cambridge University Press

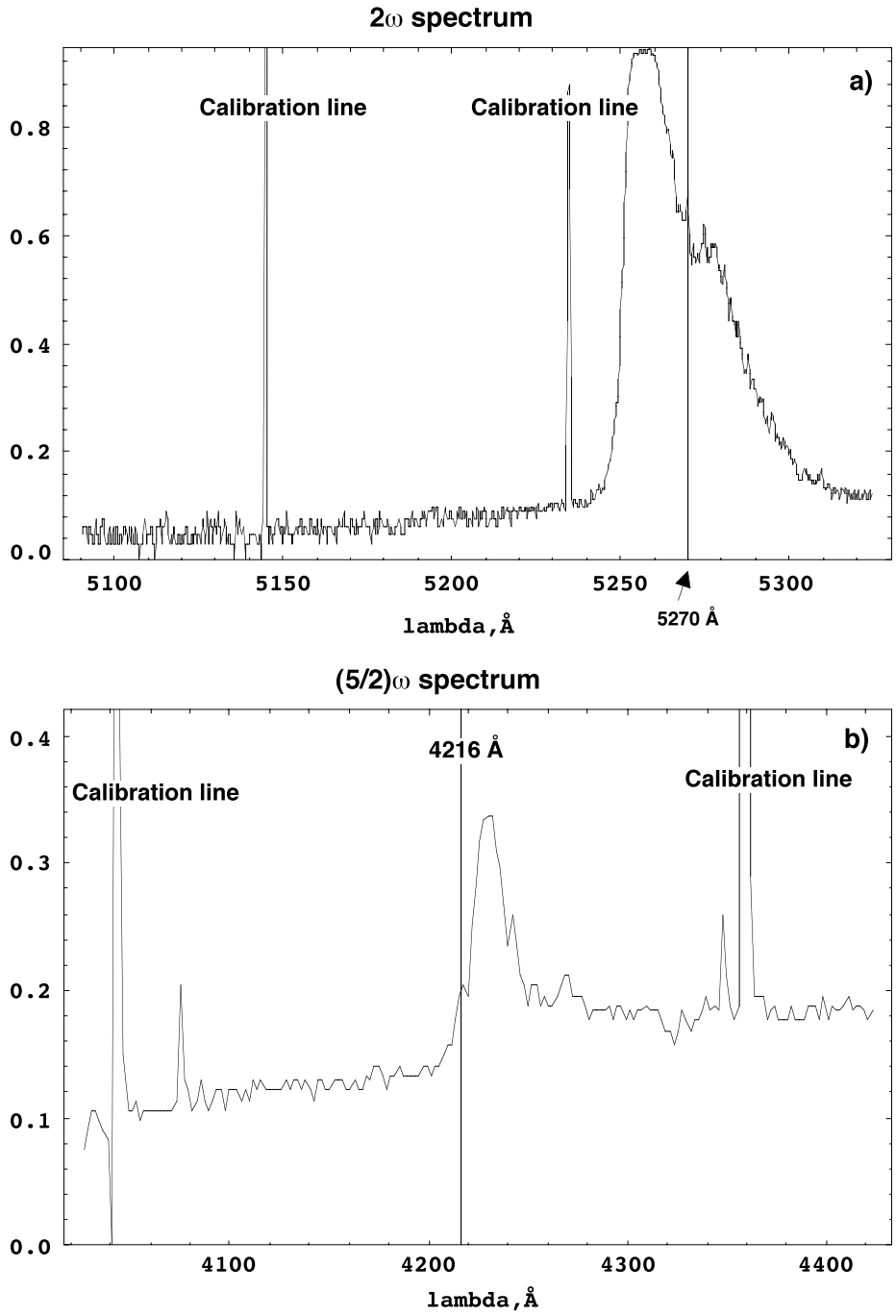

Fig. 13. (a) 2ω spectrum, taken at 60° to the normal of the target front surface. (b) $(5/2)\omega$ spectrum, taken at 60° to the normal of the target front surface.

blue and a substantial pedestal toward the red is formed. The maximum of the $(5/2)\omega$ spectrum is shifted to the red side by 14.3 Å with respect to the reference value 4216 Å.

4. ENERGY BALANCE

From the previous results it is possible to try an energy balance. In the measurements on reflected/transmitted light it was found that about 90% of the 1.054 μm laser light was absorbed (that is ≈31.5 of the laser pulse 35 J).

From the interferometric measurements at 7 ns (just after the end of the laser pulse) it was found the number of charges in the expanding plasma to be $N_{\text{etot}} \approx 8.5 \times 10^{15}$. Since from time-integrated X-ray temperature measurements T_e resulted to be about 1 keV, $N_{\text{etot}}(3/2)kT_e \approx 2$ J.

The same value results from the ionic asymptotic mean velocity of the fast component. Measured by ion collectors, this was $V_i \approx 4 \times 10^7$ cm/s, so that $N_{\text{etot}}(1/2)m_i V_i^2/Z \approx 2$ J (m_i is the average ionic mass, Z the average ionic charge).

https://doi.org/10.1017/S0263034600181042 Published online by Cambridge University Press

From the previous results it follows that a fraction $(31.5 - 2)/35 \approx 0.84$ ($\approx$30 J) of the laser light was coupled to the bulk of the target. This energy was given a part to the dense phase accelerated in the ablation-driven snowplow, and a part to the plasma filling the cavity. A fraction of this last part was ultimately transferred to the dense phase as work.

A tentative estimate for the energy of the plasma filling the cavity can be obtained as follows. Taking into account the shape factors (by comparison with simulations), the volume of the cavity can be estimated as that of an equivalent sphere of radius $R \approx V_f t$, where V_f is the snowplow velocity ($\approx 8.5 \times 10^6$ cm/s) and t the time when the laser stops ($\approx$6 ns). At this time R results to be $\approx$500 μm. The plasma density in the cavity has been evaluated to be $n_{\mathrm{ecav}} \approx 10^{20}$ cm^{-3} (see the previous section). From this follows that the thermal energy was about 13 J (at $T_e \approx 1$ keV). The remaining $30 - 13 = 17$ J was associated to that portion of the target moving at the velocity V_f (about 90%).

5. CONCLUSIONS

The experiments performed at the ABC facility of the Associazione EURATOM-ENEA sulla Fusione, in Frascati are consistent with a scenario in which efficient energy trapping in the matter occurs for laser light at 1.054 μm interacting with low density, supercritical foams (>80%). A key feature for this is the formation of a cavity where the laser light is trapped. The cavity building-up occurs through a series of nonequilibrium processes in which the matter is changed from a discrete system to a continuous one. Typical of this transition are the different ionic and electronic temperatures, shock-damping of the exploding cells (filaments) material and long duration, viscosity-damped fluid oscillations.

An ablation-driven snowplow accelerates most of the target to a velocity of the order of 8.5×10^6 cm/s, as seen from time resolved optical diagnostics. To this feature can be related the emitted ions grouping in low ($\approx 10^7$ cm/s) and high ($\approx 4 \times 10^7$ cm/s) velocity streams, as seen by ion collectors. The fast component can be associated to the ions of the plasma filling the cavity, escaping through the cavity entrance or through breaks produced by the final cavity disassembling. The slow component can be associated with the ions of the ablation-driven snowplow.

The dense phase hydrodynamic motion has been found ultimately resulting in a sort of spherical explosion, featured by tiny substructures (jets).

Diffusive heat propagation is a marginal feature in the explored regimes, being limited to the first few hundred picoseconds of the interaction when, due to the explosion and closure of the foam cell walls, also a strong nonequilibrium exists.

ACKNOWLEDGMENTS

Thanks are due to Mr. P.L. Andreoli and G. Cristofari for their excellent technical support, to Ing. A. Dattola for the continuous care to keep in healthy conditions relevant subsystems of the ABC installation, and to Dr. V.A. Pais for running the CoBi3 code for the cases displayed in this paper.

REFERENCES

Benattar, R. *et al.* 1979 *Rev. Sci. Instr.* **50(12)**, 1583.
Caruso, A. & Strangio, C. 1985 *Physics Letters* **109A(1)**, 2.
Elton, R.C. 1968 NRL Report 6738.
Gus'kov & S.Yu., Rozanov, V.B. 1997 *Quantum Electronics* **27(8)**, 696–701.
Strangio, C. & Caruso, A. 1998 *Laser and Particle Beams* **16(1)**, 45–60.